INTERFACE

royalsocietypublishing.org/journal/rsif

Research

Cite this article: Liu Y *et al*. 2023 Multiscale static and dynamic mechanical study of the *Turritella terebra* and *Turritellinella tricarinata* seashells. *J. R. Soc. Interface* **20**: 20230321. https://doi.org/10.1098/rsif.2023.0321

Received: 22 December 2022
Accepted: 10 July 2023

Subject Category:
Life Sciences–Physics interface

Subject Areas:
biophysics, biomechanics

Keywords:
impact-resistant structures, dynamic properties, bioinspired materials

Author for correspondence:
M. Tortello
e-mail: mauro.tortello@polito.it

Electronic supplementary material is available online at https://doi.org/10.6084/m9.figshare.c.6743105.

THE ROYAL SOCIETY PUBLISHING

Downloaded from https://royalsocietypublishing.org/ on 03 August 2023

Multiscale static and dynamic mechanical study of the *Turritella terebra* and *Turritellinella tricarinata* seashells

Y. Liu[1], M. Lott[1], S. F. Seyyedizadeh[1], I. Corvaglia[1], G. Greco[2,3], V. F. Dal Poggetto[3], A. S. Gliozzi[1], R. Mussat Sartor[4], N. Nurra[4], C. Vitale-Brovarone[1], N. M. Pugno[3,5], F. Bosia[1] and M. Tortello[1]

[1]Dipartimento di Scienza Applicata e Tecnologia (DISAT), Politecnico di Torino, 10129 Torino, Italy
[2]Department of Anatomy, Physiology and Biochemistry, Swedish University of Agricultural Sciences, 75007 Uppsala, Sweden
[3]Laboratory for Bioinspired, Bionic, Nano, Meta, Materials & Mechanics, Dipartimento di Ingegneria Civile, Ambientale e Meccanica, Università di Trento, 38123 Trento, Italy
[4]Dipartimento Scienze della Vita e Biologia dei Sistemi (DBIOS), Università degli Studi di Torino, 10123 Torino, Italy
[5]School of Engineering and Materials Science, Queen Mary University of London, London, UK

GG, 0000-0003-3356-7081; NMP, 0000-0003-2136-2396; FB, 0000-0002-2886-4519; MT, 0000-0002-9953-9000

Marine shells are designed by nature to ensure mechanical protection from predators and shelter for molluscs living inside them. A large amount of work has been done to study the multiscale mechanical properties of their complex microstructure and to draw inspiration for the design of impact-resistant biomimetic materials. Less is known regarding the dynamic behaviour related to their structure at multiple scales. Here, we present a combined experimental and numerical study of the shells of two different species of gastropod sea snail belonging to the Turritellidae family, featuring a peculiar helicoconic shape with hierarchical spiral elements. The proposed procedure involves the use of micro-computed tomography scans for the accurate determination of geometry, atomic force microscopy and nanoindentation to evaluate local mechanical properties, surface morphology and heterogeneity, as well as resonant ultrasound spectroscopy coupled with finite element analysis simulations to determine global modal behaviour. Results indicate that the specific features of the considered shells, in particular their helicoconic and hierarchical structure, can also be linked to their vibration attenuation behaviour. Moreover, the proposed investigation method can be extended to the study of other natural systems, to determine their structure-related dynamic properties, ultimately aiding the design of bioinspired metamaterials and of structures with advanced vibration control.

1. Introduction

Over millions of years of evolution, biological systems have developed mechanical, optical and thermal properties that aid their fitness by solving specific needs. Regarding the mechanical properties, a rich literature can be found dealing with the remarkable quasi-static properties of many natural systems [1–4]. On the other hand, the dynamic mechanical properties of biological systems are, up to now, less explored, although a collection of several notable examples can be found in recent review papers [5,6].

Marine shells, and in particular their micro- and nano-structure, have long been studied as ideal material systems for mechanical protection [7] and impact attenuation [8], and have also been a source of bioinspiration for impact-resistant materials [9]. There are approximately 60 000–70 000 species of shell molluscs, the two largest classes being the Gastropoda and the Bivalvia. The molluscan shell is secreted by the mantle, or pallium, that is the epithelial layer covering

© 2023 The Author(s) Published by the Royal Society. All rights reserved.

Downloaded from https://royalsocietypublishing.org/ on 03 August 2023

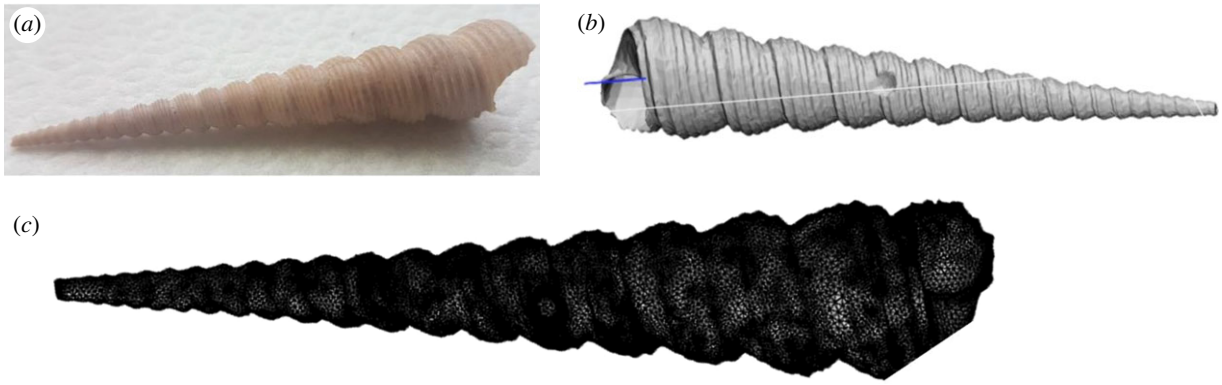

Figure 1. (*a*) *Turritella terebra* sample. (*b*) Three-dimensional representation from stereolithography (STL) file of *Turritella terebra* generated by µCT scan. (*c*) Modified *Turritella terebra* STL file suitable for FEA.

the molluscs [10]. The shell growth starts by the gland of a larval shell (the protoconch) and proceeds by the addition of new rings of conchiolin impregnated with calcium carbonate to the edge of the shell, and by addition of calcium carbonate over the whole of its inner surface and a small number of organic matrices [11]. Calcium carbonate has three crystal polymorphs: calcite, aragonite and vaterite, in addition to an amorphous form [12]. Calcite is the most stable of the three polymorphs under ambient conditions, whereas aragonite is metastable and vaterite is the most unstable. Most mollusc shells consist of aragonite and/or calcite, whereas vaterite is rarely found. Usually, the secreted calcareous material is in the crystalline form of prisms of calcite arranged normally to the surface of the shell, whereas the inner part is made of layers of crystals of aragonite parallel to the shell surface. There are several types of microstructures, like the nacreous, the crossed lamellar, the foliated and the prismatic layer microstructures [13–15]. The calcium carbonate structural elements form at least 95% of the shell making them stiff and strong, while the remainder consists of biopolymeric material that helps to make them tough as well [16]. Although the nacreous and prismatic layer structures are most extensively studied, the most abundant microstructure in molluscs is the cross-laminar one. The thin lamellar prisms of approximately 100 nm thickness, called third-order lamellae, are aligned parallel and create the plate (second-order lamellae) that inclines at an angle of approximately 45° against the shell surface. This microstructure has a particularly high ceramic content (up to 99.9% in mass), yet it shows unusually good mechanical performance [17–19]. Nacre features the highest tensile and compressive strength among the various architectures, while the crossed lamellar has the highest fracture toughness [7]. Its functional features are intimately associated with the microstructure of the shell, which is usually formed by three layers: inner (close to the animal), middle and outer. When the shell undergoes a quasi-static load caused, for example, by the bite of a predator, the outer layer experiences multiple cracks that are stopped at the interface with the middle layer. With increasing load, damage also starts propagating inside the middle layer, but bridging forces, created by the particular orientation of the internal lamellae, hinder crack propagation [20]. Moreover, different microstructural responses have also been reported, depending on the velocity of the impacts, generating different mechanisms of attenuation and fracture formation, showing in some cases a considerable enhancement of the dynamic fracture strength with respect to that of quasi-static loading [8].

Numerous examples of efficient vibration damping structures exist in nature [6]. Some well-known cases are the Mantis shrimp dactyl club [21], the woodpecker skull [22] and the turtle shell [23]. A common feature of these examples, which is also found in seashells, is the multiscale (hierarchical) organization of the structure, from optimized microstructures combining stiff and compliant components, to vibration-deflecting or attenuating elements at intermediate scales (e.g. oriented fibre bundles, suture joints) [5,24–26], to tuned resonance properties at full scale, e.g. occurring far from typical working conditions. Ultrasonic techniques, in particular resonant ultrasound spectroscopy (RUS) [27,28], have successfully helped to determine and investigate the macroscopic mechanical properties on several biological samples including wood [29,30], bones [31,32], or the human skull [33], also in combination with micro-computed tomography (µCT) scans and finite element analysis (FEA) [34], while nano and microscale characterizations are also fundamental to address the same properties at smaller length scales [35–39].

While, as reported above, it is well known that the microstructure in shells plays a fundamental role in impact attenuation, their overall shape also determines their modal characteristics and vibration damping capabilities that can, at least partially, be related to the main function of the shell. This has been shown for example in a quasi-static analysis of the *Otala lactea's* shell where its complex and curved geometry has been demonstrated to have an important role in enhancing the protective role of the mollusc shell from a mechanical point of view [40]. However, we are not aware of dynamic studies performed on this kind of systems.

In this paper, we focus on two shells belonging to the Turritellidae family, namely the *Turritella terebra* (Linnaeus, 1758) and the *Turritellinella tricarinata* (Brocchi, 1814). They are among the most common and abundant species on muddy and sandy seafloors, which are typical far from the coasts. Often, they are the dominant species, with hundreds of individuals per square metre. Both shells are characterized by a long tower-like shape which resembles a drill, as shown in figure 1, hence the name. This long and narrow helicoconic shell shape may also facilitate, through the foot, the access of the mollusc under the soft mud and anchoring to the marine substrate to prevent deep currents from carrying away the shell. Several structural features of *Turritella terebra* have been investigated in order to learn from nature, e.g. for the design of 'adaptable structures', since this shell grows in an adaptive way and is able to change form through time to meet performance demands [41–43]. Mathematical models of the shell have been proposed and finite element analysis has also been performed [43,44]. The shells have three

Downloaded from https://royalsocietypublishing.org/ on 03 August 2023

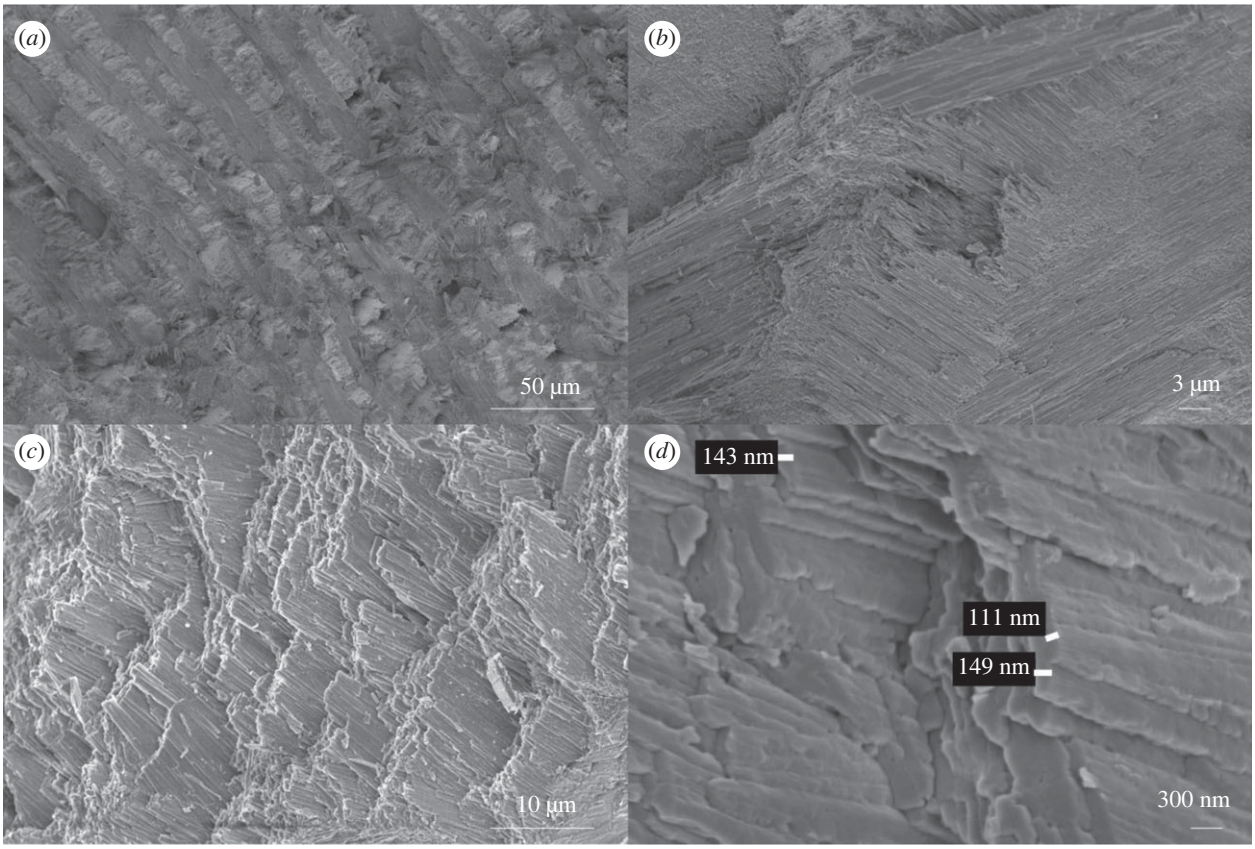

Figure 2. SEM images of the *Turritella terebra* shell. (*a*) First-order lamellae approximately 10 µm thick with alternating orientations of the second order lamellae. (*b*) Second-order lamellae stacked in groups forming different angles with respect to each other. (*c,d*) Third-order lamellae with thickness ranging from approximately 100 to 150 nm.

macroscopic layers, called the inner, middle and outer layer, but it is not clear whether the calcium carbonate crystals are in the form of calcite or aragonite [43]. Each is organized in the crossed lamellar architecture showing, from the largest to the smallest scale, the first-, second- and third-order lamellae.

Here, we present a multiscale study of the mechanical properties of these two shells. By applying a combined numerical and experimental procedure at the micro and macro scale, we investigate the complex architecture of the shells and determine global mechanical properties studying their modal response and vibration properties. Their frequency response spectra are then compared with simulated ones and discussed in terms of possible vibration attenuation capabilities, in the perspective of providing useful elements for the design of bioinspired metamaterials with engineered wave propagation properties.

2. Material and methods

In the following, we will describe the techniques and procedures used for the investigation of the two shells. The μCT scan and the subsequent use of a specific software for the elaboration of the obtained images allowed to characterize the geometry of the shell that could be imported in a finite-element software. The electron microscope was employed to directly determine the microstructure of the shells while the atomic force microscopy (AFM) allowed to obtain the spatial distribution of the Young's modulus at the nanoscale along with the topography characterization of the polished surface of the samples. The obtained results were supported by further instrumented nanoindentation measurements. RUS experiments were performed to characterize the vibrational properties of the overall structure of the samples and numerical FEA was used to retrieve the mechanical properties of the samples from the experimental results and to further investigate their vibration attenuation capabilities.

2.1. Micro-computed tomography scan and creation of a three-dimensional mesh for finite element analysis

CT scans of the shell were performed by using the three-dimensional X-ray microscope Skyscan 1272 by Bruker. The images allowed us to obtain a clear three-dimensional view of the sample geometry. The outcome of this experiment was a triangulated stereolithography (STL) file which was generated based on pixel density, as shown in figure 1*b*. STL files of the samples were prepared according to the procedure suggested by Bruker for the three-dimensional scan. For the FEA, the STL files were then re-meshed to reduce the mesh density and imported into Meshmixer v. 3.5 software, where different operations such as Hole Filling, Auto Repair, Mesh Smoothing, Mesh Solid and Remesh were used. This process was repeated several times to remove intersecting triangles, reduce the number of triangular elements and general errors in the file. The initial number of nodes was ranging between approximately 400 thousand and 1.5 million, depending on the case, and the density after re-meshing was 8–10% of the initial one. The modified three-dimensional STL file, reported in figure 1*c*, was then imported into a FEA software (COMSOL Multiphysics 6.0) for further simulation and analysis.

2.2. Scanning electron microscopy

SEM images of the sections of the two types of shell were acquired after mechanical fracturing of the samples. A Merlin field emission scanning electron microscope by Zeiss was used to obtain several images of the microstructure. Figure 2 shows

Downloaded from https://royalsocietypublishing.org/ on 03 August 2023

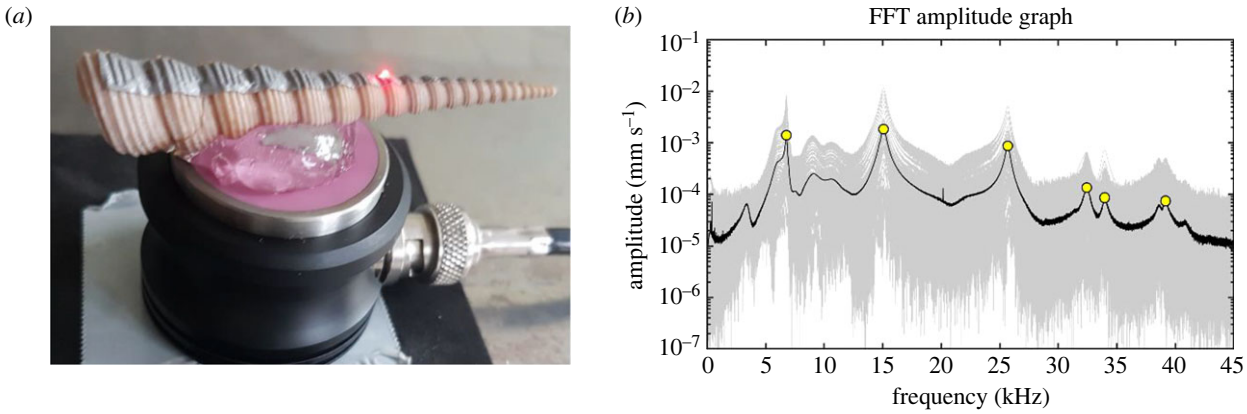

Figure 3. (*a*) TT sample mounted on the transducer during ultrasonic excitation experiments. (*b*) Grey lines are the frequency spectra recorded along the longitudinal axis of the shell while the black line represents their average. Yellow symbols represent the resonance frequencies.

some images of the *Turritella terebra* shell at different magnification levels. In panel (*a*) it is possible to observe a layered structure formed by the first-order lamellae, each with a thickness of a few micrometres (less than 10 µm). Further magnification, panel (*b*), indicates that each layer is formed by lamellar elements with different orientations depending on the layer. Panels (*c*) and (*d*), show a magnification of the calcium carbonate lamellae forming the various layers. Each sub-element, corresponding to a third-order lamella, is approximately 100–150 nm thick.

Similar images were acquired also for the *T. tricarinata* sample and are reported in the electronic supplementary material. The same cross-laminar architecture was observed. Sometimes (as shown in electronic supplementary material, figure S1c), some elements featuring a rod-like shape were also observed. However, in both cases, a clear, crossed lamellar, structured composition of the shell was revealed.

2.3. Atomic force microscopy

In order to measure the local mechanical properties of the *Turritella* shells, AFM experiments were conducted, allowing to obtain, by analysing the force curves, the distribution of the elastic modulus on the sample surface. An Innova atomic force microscope by Bruker was used for the acquisition of the force versus distance curves. A hand-crafted ultra-high force probe (Bruker DNISP-HS) fabricated by precision grinding of a solid diamond with tip radius of 40 nm and tip half angle 42.3° was used. Sensitivity calibration of the AFM probe was done by using a sapphire sample, and the reliability of the Young's modulus determination was verified on a fused silica test sample (electronic supplementary material, figure S2). The probe is specifically designed for nanoindentation and its stiffness, $k = 353$ N m^{-1}, is ideal for the expected range of Young's modulus of this sample (calcium carbonate).

Turritella samples were embedded in epoxy resin and polished with sandpaper up to 4000 grit, and subsequently with a 1 µm diamond paste to obtain a flat surface on which to acquire the force curves. Even if the roughness of the polished surface is of the order of 4 nm, the effect of the microstructure cannot be avoided as the sample itself is not a bulk material, but it is formed by calcium carbonate lamellae.

2.4. Instrumented nanoindentation

To perform the tests on the shells, we used an established protocol [45]. The shells were broken and fixed into an epoxy resin, which was left to dry for 24 h. The samples were then polished to achieve a roughness of approximately 40 nm. Three types of samples were produced: *Turritella terebra* (samples named TT0 and TT) and *Turritellinella tricarinata* (sample named TC1). We performed nanoindentation tests with the support of an iNano nanoindenter (Nanomechanics Inc.). The declared sensitivity of the machine is 3 nN for the load and 0.001 nm for the displacement. The shell was analysed by means of mapping method (Nanoblitz 3d, Nanomechanics Inc.). This gives the distribution of the mechanical properties of the sample on a specific squared area of interest (selected with the support of the coupled optical microscope). For each map, 40/50 × 40/50 points were investigated. A Berkovich tip, i.e. with a three-sided pyramidal shape, was mounted in the machine and used to perform the experiments (at controlled temperature and humidity, 20°C and 30–40% RH); the method in Oliver & Pharr [46] was used to compute the mechanical properties, with indentation loads in the range 0.1–0.5 mN.

2.5. Ultrasonic measurements

RUS experiments were performed by applying chirp signals in the 1–45 kHz frequency range to the TT sample, by using a 500 kHz Olympus piezoelectric transducer, as shown in figure 3*a*. Water gel was used as a coupling medium. The out-of-plane output vibration signal was recorded by means of a laser doppler vibrometer (Polytec) on 60 points along the longitudinal axis of the shell, previously carefully covered by reflective tape. The laser scan of the surface was automated by using a translational motor stage. The experimental set-up chosen for this measurement is characterized by an excitation probe with larger mass and dimensions than the object under study. This choice is dictated by the desire to study global resonances of the structure without studying transient wave propagation or local resonances. Panel (*b*) reports, as grey lines, the 60 spectra recorded during the measurements along with the average spectrum, indicated by the black line. The spectra differ mainly in the attenuation levels, in the level of noise, and relative spectral weight of the main peaks, but it is possible to recognize main common features that can be traced back to the entire structure. This justifies the study of the average spectrum of the sample. The average spectrum clearly shows several resonance modes of the structure that can be investigated further and suitably compared with FEA simulations. Since we are addressing the lowest order modes of the shell, it can be reasonably expected that changing positioning and orientation of the shell with respect to the transducer will possibly change the relative magnitude of the resonance peaks in panel (*b*), but not the overall average spectrum.

3. Results

3.1. Atomic force microscopy results

Figure 4*a* shows a camera image of the polished *Turritella terebra* sample, called TT, and the microstructure is still visible on

Downloaded from https://royalsocietypublishing.org/ on 03 August 2023

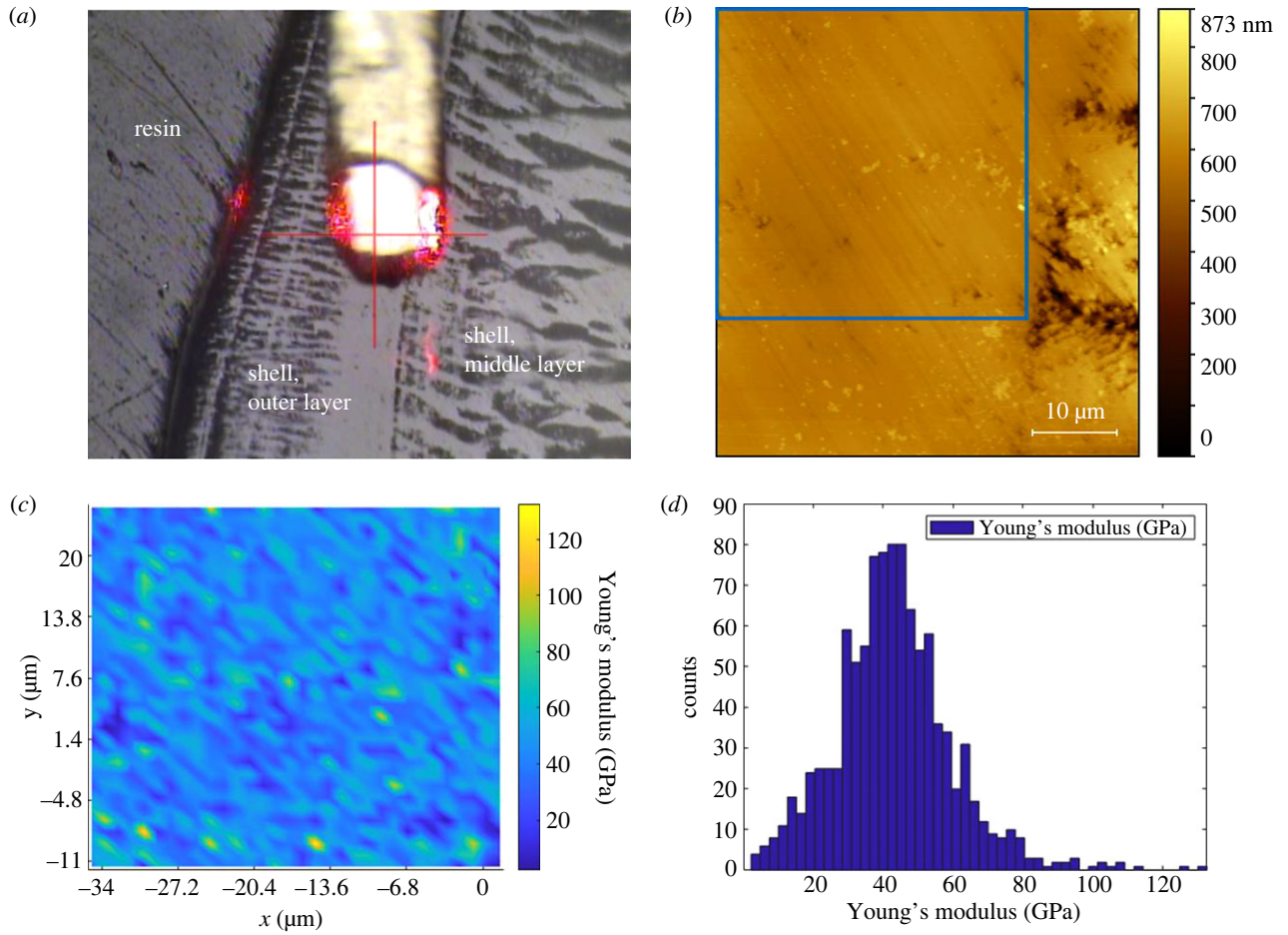

Figure 4. (*a*) Camera image of the sample and cantilever before acquisition of topography images and force versus distance curves on the TT shell embedded in resin. (*b*) Topography image of TT surface. (*c*) Young's modulus map of the area located by the blue square of panel (*b*). The values were calculated by analysing the force curves obtained by using the AFM in the force-volume mode. (*d*) Distribution of the obtained Young's modulus values reported in the map shown in (*c*).

the right-hand side of the image, where the first-order lamellae, like those shown in figure 2*a*, can be seen. A topography image of the polished surface, recorded on a flat area, is reported in panel (*b*). The topography image mainly shows the edge between the outer (flat) and middle (more irregular) layer of the shell. The right-hand side of the surface shows some holes and voids in the microstructure, that were probably caused by the polishing procedure or by an intrinsic defect, but the remaining surface appears rather smooth. After recording the topography image, a matrix of 32×32 force versus distance curves was acquired in the area located by the blue square. The maximum force was set around 30 µN. Since the sample is hard and the adhesion force is very small compared with the maximum applied force and thus negligible, we fitted the approach curves by using the elastic Hertz model [47,48], as also done in [49].

Each force–displacement curve was analysed by implementing the Hertz model in MATLAB and using the approach curve for the fitting procedure. The corresponding Young's modulus value was plotted in the location where the curve was acquired, as shown by the colour map of figure 4*c*. The moduli were calculated from the reduced ones by using the properties of the diamond tip ($E =$ 1140 GPa and $\nu = 0.2$) and by assuming, only relative to this analysis, the Poisson's ratio of the shell approximately equal to $\nu = 0.3$, obtaining a rather large dispersion of the values. This is due to the underlying microstructure of the shell, as clearly highlighted by the SEM measurements. The expected range of the Poisson's ratio for the calcium carbonate is 0.3–0.33, and a variation within this range is inside the experimental uncertainty. Panel (*d*) reports the distribution of the obtained values, whose average is in the expected range [50] and equal to $E = 43 \pm 17$ GPa. No significant variations, within the error bars, are observed along the cross-section of the shell. The underlying microstructure, and the consequent dispersion of the obtained values, hinder the possibility of detecting, on such length scales, local variations of the mechanical properties of the shell in the different layers because the AFM is probing the $CaCO_3$ crystals along with the lamellar interfaces. Therefore, we cannot exclude the presence of anisotropy (both in the Young's modulus and Poisson's ratio) in the different layers but, if present, it must be smaller than the experimental uncertainty, since the microstructure of the sample makes it impossible to have continuous flat surfaces at the nanoscale. The fact that inside the first- and second-order lamellae the elements are arranged in different orientations according to the crossed lamellar microstructure, indicates that tests normal to the layers, also given the large error bars, should not offer new insights for the anisotropy by using these techniques. As for the third-order lamellae, which consist of calcium carbonate crystals (figure 2*c* and *d*), they should feature some degree of anisotropy in the Young's modulus due to the different crystalline orientation [51,52]. However, to detect it, atomically flat, single-crystal samples should be used for the experiments.

Downloaded from https://royalsocietypublishing.org/ on 03 August 2023

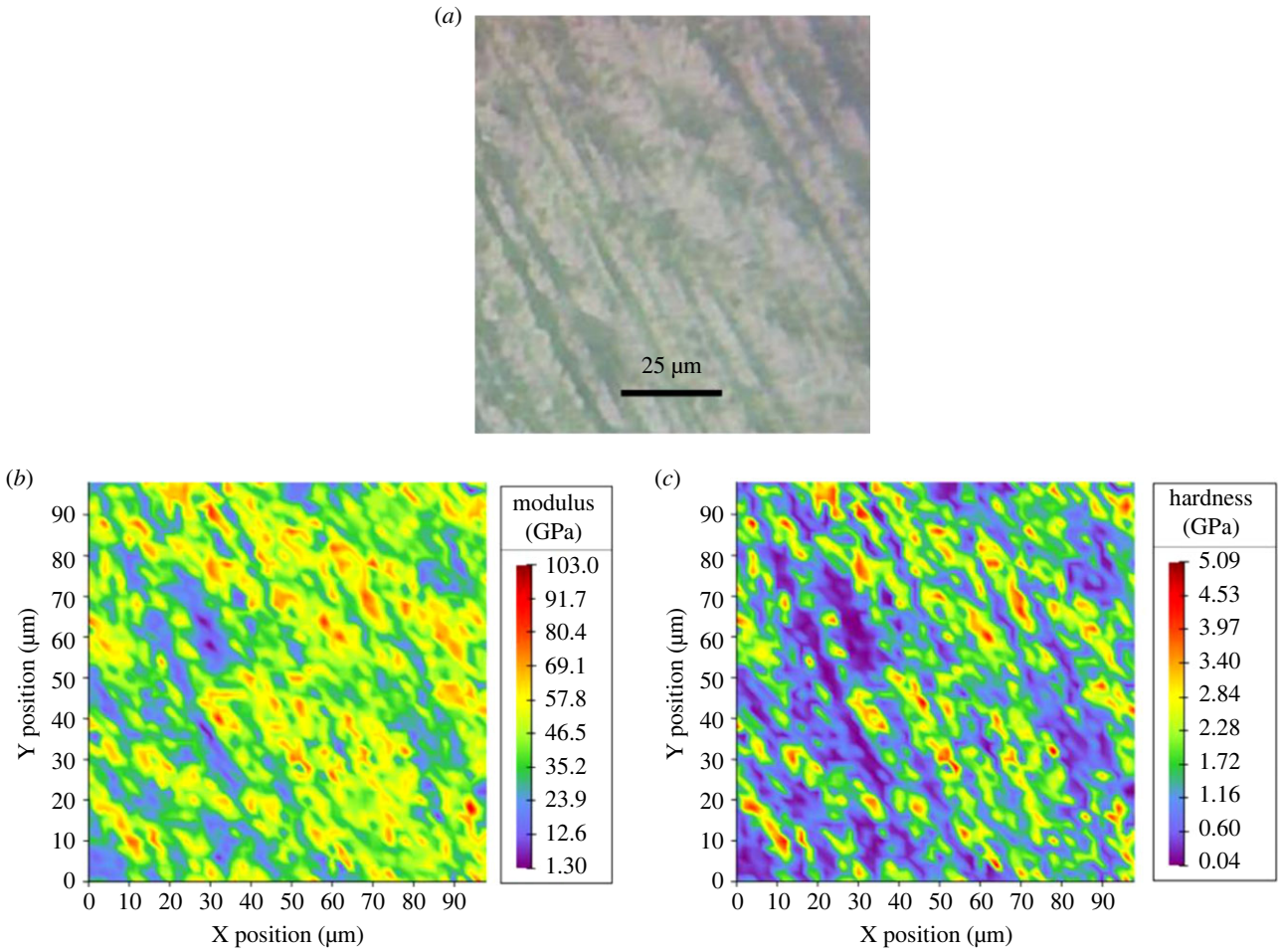

Figure 5. (*a*) Representative light microscopy image of the region of interest for which are reported (*b*) Young's modulus and (*c*) hardness map. The sample depicted here is TT0. For these experiments the maximal load of 0.1 mN was used.

Nevertheless, we know that it is the composite [9] and multiscale structure [20], according to which the lamellae are placed with different relative orientations, the reason of their exceptional impact-resistance properties. Therefore, the macroscopic mechanical properties of the shell are the results of a complex, multiscale microstructure, that is not just the sum of the single components and that gives rise here to a wide dispersion of data in the force–displacement curve results.

Topography scans on smaller areas, reported in the electronic supplementary material, were able to reveal the underlying microstructure. A Young's modulus map on a $2 \times 2\ \mu m^2$ area of a *T. tricarinata* sample TC1, shows that there is no clear spatial correlation between the topographic features and the Young's modulus values (electronic supplementary material, figure S3). However, the effect of the microstructure is reflected also in this case in the rather large dispersion of data. In this case, the obtained value was $E = 48 \pm 17$ GPa. The standard deviation of the distribution is the same as that obtained on the $36 \times 36\ \mu m^2$ area shown in figure 4. Since the dispersion of data is considerable, the difference with respect to the previous sample is not statistically significant. Therefore, the AFM investigation is not essential to determine the effective Young's modulus of the structure, but rather to highlight its inhomogeneity at this scale due to the lamellar structure (revealed by the SEM measurements) and to have a first guess for determining the mechanical properties of the overall system.

Topography scans with a probe specifically designed for imaging (Bruker RTESPA-300, nominal curvature radius = 8 nm) were also performed to gain a clearer idea of the appearance of the underlying microstructure, even in the case of very smooth surfaces. An example is reported in electronic supplementary material, figure S4. The topography, but especially the phase, show very well that the material is formed by many elements that, as seen in the SEM images, have a lamellar form but that here appear as sort of 'tiles' or grains forming the structure.

3.2. Nanoindentation results

To compare the previous results with those obtained by a different characterization technique at the nanoscale, instrumented nanoindentation experiments were also conducted. Here, the main difference is that the force is not applied by means of a cantilever, but vertically, thus providing very accurate measurements when probing bulk or porous regions, like the interface between different lamellae. Although it is not possible to obtain the topography of the surface with this method, nanoindentation allows to obtain an estimation of the mechanical properties of the single elements forming the microstructure, while the AFM, as reported above, rather highlights the complex microstructure.

No significant gradients of the mechanical properties were observed in the analysed cross-sections of the shells (figure 5). As shown below, this supports the approximation used in FEA simulations of considering constant homogeneous mechanical properties over the whole sample. In the indentation region, empty spaces were found that indicate a similar 'porous'

Downloaded from https://royalsocietypublishing.org/ on 03 August 2023

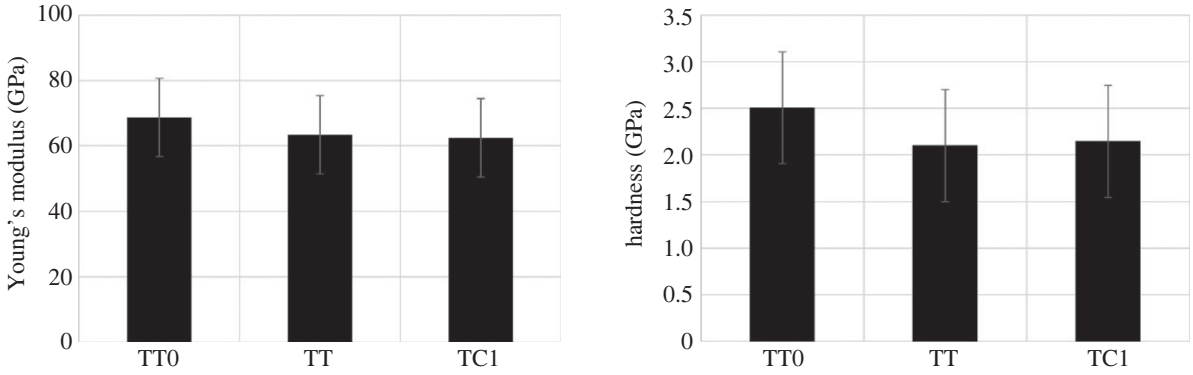

Figure 6. Young's modulus and hardness of the tested TT and TC samples. These values were selected from the maps reported in electronic supplementary material, figure S6 considering values with hardness greater than 1.5 GPa, and Young's modulus greater than 50 GPa to avoid the empty regions. No significant differences emerge among these values.

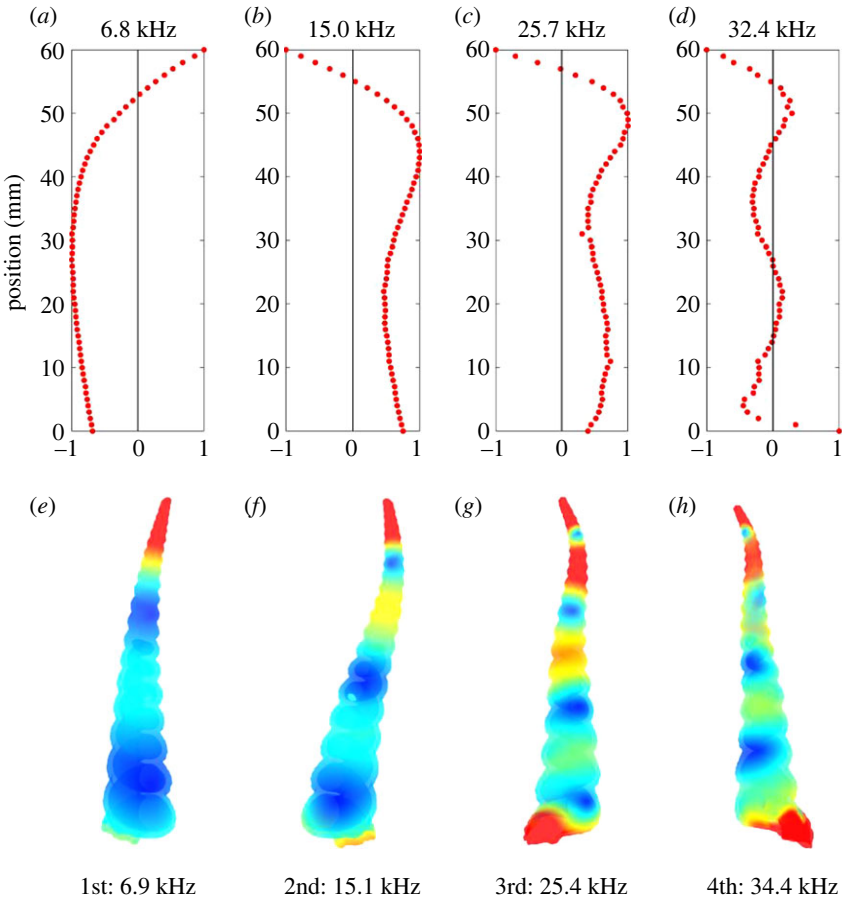

Figure 7. (*a–d*) Experimental normalized modal shapes for some of the main resonance frequencies for the TT sample. (*e–h*) Vibration modes obtained by finite-element simulations after optimization of the material parameters (see main text for details).

structure (figure 5 and electronic supplementary material, figure S6), due to the microstructure of the shell. The analysis was then focused on the edge between the resin and the shell cross-section.

As reported in figure 6, the overall values of the Young's modulus and hardness were not significantly different among TT0, TT and TC1 samples, which all displayed a rather large scatter in the data due to the porosity and roughness of the surface. In this case, it is possible that such dispersion screens small differences in the values of the mechanical properties among the different samples, thus requiring a more precise technique.

3.3. Ultrasound experiments results

Panels (*a–d*) of figure 7 report, for some of the main observed resonance peaks, the normalized experimental modal shape along the longitudinal axis of the shell. This was obtained by plotting, at the frequency of the selected resonance mode, the imaginary part of the fast Fourier transform (FFT) as a function of the laser spot position, reported in the vertical axis as mm, that spanned over the entire length of the shell. This allowed to appreciate the amount of bending of the structure as a function of the position. The maximum value was normalized to one. Since out-of-plane vibrations

Downloaded from https://royalsocietypublishing.org/ on 03 August 2023

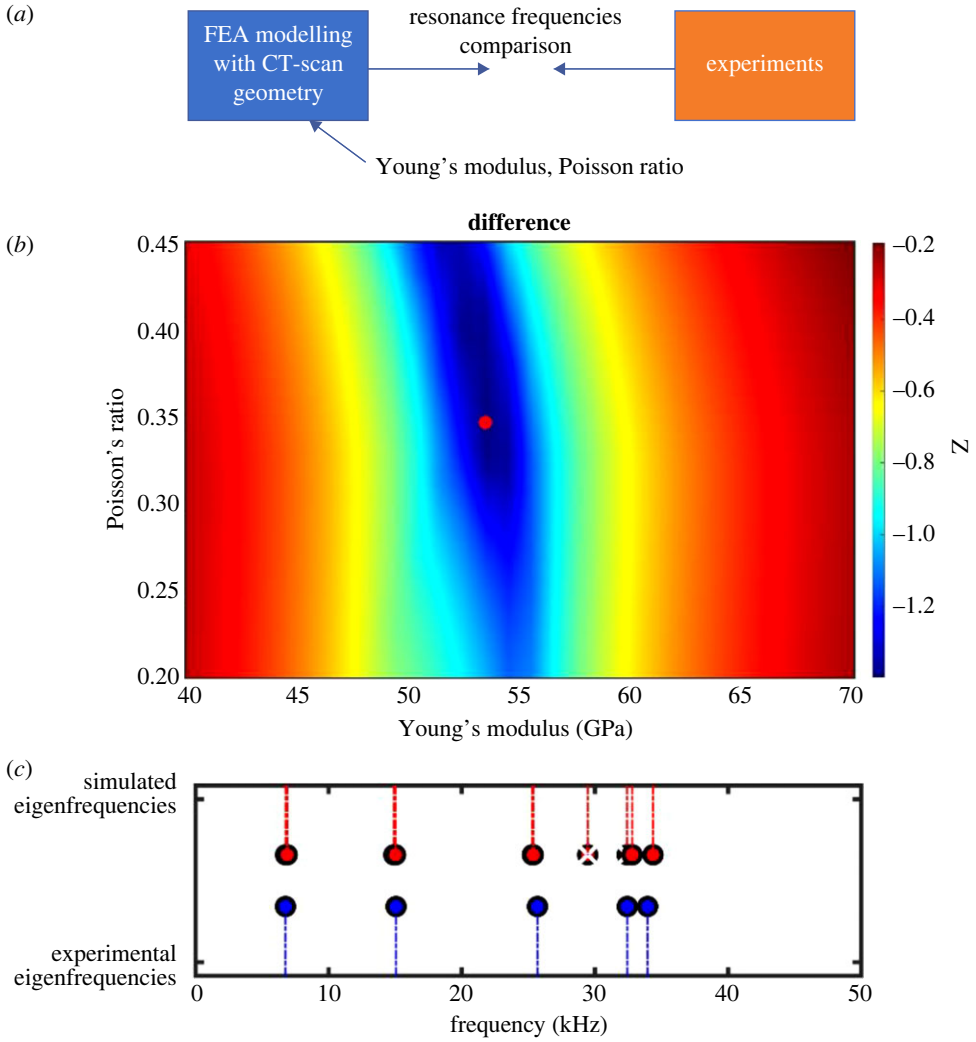

Figure 8. (*a*) Schematic of the comparison between FEA and experiments. (*b*) Colour map of the difference between experiment and simulation for the first four resonance modes as a function of the material parameters (Young's modulus and Poisson ratio) for the TT shell. The red dot represents the point that best matches experiments and simulation for all the resonances considered. Outside the reported range of Young's modulus, the agreement between experiment and simulations is poorer. (*c*) Comparison between experimental and simulated eigenfrequencies.

were probed, the reported modes are predominantly bending modes.

Panels (*e–h*) of figure 7 show the corresponding eigenmodes obtained by FEA using the material parameters that best match the experiments, as explained below in more detail. Considering that, from the experimental point of view, only bending modes can be detected, there is a good agreement between experiments and simulations both in terms of the modal shapes and corresponding resonant frequencies.

Similar measurements were also performed on two samples of *Turritellinella tricarinata*, TC1 and TC2, in the 5–100 kHz range. Results are reported in electronic supplementary material, figures S7 and S8. In these cases, some resonance peaks are visible at higher frequencies than observed in the previous sample, given the smaller size of these two shells.

3.4. Finite element analysis-based resonant ultrasound spectroscopy

Resonance frequencies and mode shapes were calculated by using COMSOL Multiphysics 6.0 after importing the processed three-dimensional geometry obtained from the CT scan. The eigenfrequencies were computed as a function of the Young's modulus and Poisson's ratio of the material by using the Structural Mechanics module and by performing an eigenfrequency study with parametric sweeps. The range of the swept parameters was initially chosen to include, as first guess, the values obtained from the mechanical characterization at the nanoscale. In this regard, it is worth pointing out that single, isotropic values for the Young's modulus and Poisson's ratio were used. The assumption of neglecting the complex (hierarchical) crossed lamellar microstructure shown in figure 2 is justified mainly due to two aspects: (i) from a theoretical point of view, the features typically observed in the microstructure present dimensions many orders of magnitude smaller than the whole system, such that interference phenomena (e.g. Bragg scattering) occur at significantly higher frequencies than the ones considered in the finite-element analysis; and (ii) a computational limitation, as an impractical amount of memory would be required to obtain simulation results from even the simplest analysis, due to the number of elements necessary for the proper discretization of the system. Moreover, as we have seen, the microstructure of the shell does not allow to highlight any anisotropy, and the dispersion of the obtained values is rather large. This is the reason why the experimental values were used only as an initial guess.

The calculated eigenfrequencies and relevant mode shapes were then compared with the experimental ones (figure 8*a*).

Downloaded from https://royalsocietypublishing.org/ on 03 August 2023

A certain number n of eigenmodes was considered and the optimized material parameters were determined as those minimizing the function

$$Z = \log\left(\sum_{i=1}^{n}\left|\frac{(f_i^{\mathrm{exp}} - f_i^{\mathrm{sim}})}{f_i^{\mathrm{exp}}}\right|\right), \tag{3.1}$$

where f_i^{exp} and f_i^{sim} are the experimental and calculated eigenfrequencies of the i-th mode, respectively. The abscissae and ordinates of the colour map reported in figure 8*b* show, for the TT sample, the investigated range of Young's modulus and Poisson's ratio values, respectively, while the colours indicate the value of Z, which in this case has been computed by considering the first four resonance modes ($n = 4$). The red dot locates the minimum Z value corresponding to the optimized parameters that, in this case, turn out to be approximately $E = 53 \pm 2$ GPa and $\nu = 0.35 \pm 0.06$, where the uncertainties are calculated by propagating the error of f_i^{exp} and f_i^{sim} to Z. Figure 8*c* compares the experimental and simulated eigenfrequencies. The broken symbols indicate simulated modes with a dominating longitudinal displacement which, therefore, cannot be efficiently experimentally detected by the vibrometer, sensitive to the out-of-plane displacements only. Notice that there are two such modes, as the second, around 33 kHz, is almost superimposed to another one.

In the case of the two *T. tricarinata* samples, three frequencies were considered in the minimization process, from which we obtained $E = 70 \pm 2$ GPa and $\nu = 0.32 \pm 0.05$ for TC1 and $E = 61 \pm 3$ GPa and $\nu = 0.31 \pm 0.09$ for TC2, respectively. Results are reported in electronic supplementary material, figures S9 and S10. By looking at images shown in figure 8*b* and electronic supplementary material, figures S9a and S10a, we can notice that the variation of Z is greater when driven by the Young's modulus rather than by the Poisson ratio. Thus, the Young's modulus is a much more relevant parameter in the inversion procedure for determining the mechanical properties of the samples, indicating that only this quantity should be compared at the different investigated length scales. The Young's modulus values obtained in the three cases are all within the range determined by the nanoindentation experiments (figure 6), but we can now appreciate some differences, as dissimilarities in the mechanical properties, that can be due to individual variability. Indeed, it is known that environmental and ecological conditions, like sea temperature and oxygen concentration, may affect the elemental composition and isotopic ratio in the mollusc shell [53–56]. This could be the rationale for future work, in which a large amount of specimens of the same species but with different ecological history could be analysed.

If we compare the obtained elastic moduli with those reported in the literature for different seashell microstructures [57,58], we can see that for the nacreous structure they are in the 40–60 GPa range, while for the crossed lamellar one they are in the 40–80 GPa range. For the foliated structure, values in the 30–40 GPa range are given, and for the prismatic one they are around 20 GPa, although fewer species were tested for this structure. Therefore, the crossed lamellar structure is the stiffest. Although it was found that the nacreous structure has a higher strength in tensile and bending tests, the crossed lamellar structure is the most widely studied. The main method used for measuring the elastic moduli of different shell structures is the three-point bending test. Our results are well within the reported range for the crossed lamellar microstructure. In particular, they have been obtained by using RUS, which makes use of the scanned geometry and where isotropic values for the elastic constants were assumed.

4. Discussion

4.1. Frequency domain response

After having characterized the mechanical properties of the shells and shown that they agree with previous studies, to better understand the dynamic behaviour of the structure of the *Turritella* shells, we performed a comparative numerical frequency domain analysis using the obtained mechanical data. The actual geometry, obtained from the CT scan, was used to compute the frequency response spectrum in a certain frequency range. The damping was modelled using an isotropic loss factor η_s (defined as the ratio of energy dissipated in unit volume per radian of oscillation to the maximum strain energy per unit volume). This value was estimated by comparing the simulated particle velocity field as a function of frequency with the experimentally derived one in the range 0.5–100 kHz. The computed spectra are reported in figure 9 for different loss factor values, along with the experimental data for sample TC1. It is apparent that the addition of damping considerably improves the agreement with the experimental data, although there is some discrepancy between peak amplitudes at some resonance frequencies. For example, the experimental peak at 20 kHz is rather damped, but the one at approximately 65 kHz is still clearly noticeable. This can be related to the out-of-plane nature of the measurements, which can introduce some differences in the measured relative peak intensities, as well as in the number of detected peaks. A loss factor of $\eta_s \approx 5 \times 10^{-3}$–$1 \times 10^{-2}$ reproduces the experimental data well, since for larger values (as in the case of $\eta_s = 3 \times 10^{-2}$, also shown in the figure) some spectral features are lost.

4.2. Vibrational properties and comparison with other structures

To understand the influence of the full *Turritella* structure on its modal vibration properties, we then compared its frequency response with that of a similar, but simpler, ideal structure. The *Turritella* structure is helicoconic and the internal hollow spiral structure, in comparison with a basic conical one, can presumably provide better structural strength and impact damping to protect the living organism from predators. Moreover, it also presents a hierarchical organization, since every spiral contains, on its surface, several thinner spirals that curl around the larger ones. Therefore, it is interesting to compare this structure with its simplest analogue, where only the conical shape has been retained. This can help to better understand the influence on the mechanical behaviour of 'second-order' elements in the hierarchical structure. The geometry of the conical structure was designed to have the same mass and length as the *Turritella* shell used for the comparison. The density, Young's modulus, Poisson's ratio and loss factor were the same in both cases. Figure 10 reports the vibration strain energy as a function of the frequency for these two systems. Results show that, for the two structures, the modes at frequencies up to 80 kHz are essentially the same. This is clearly due to

Downloaded from https://royalsocietypublishing.org/ on 03 August 2023

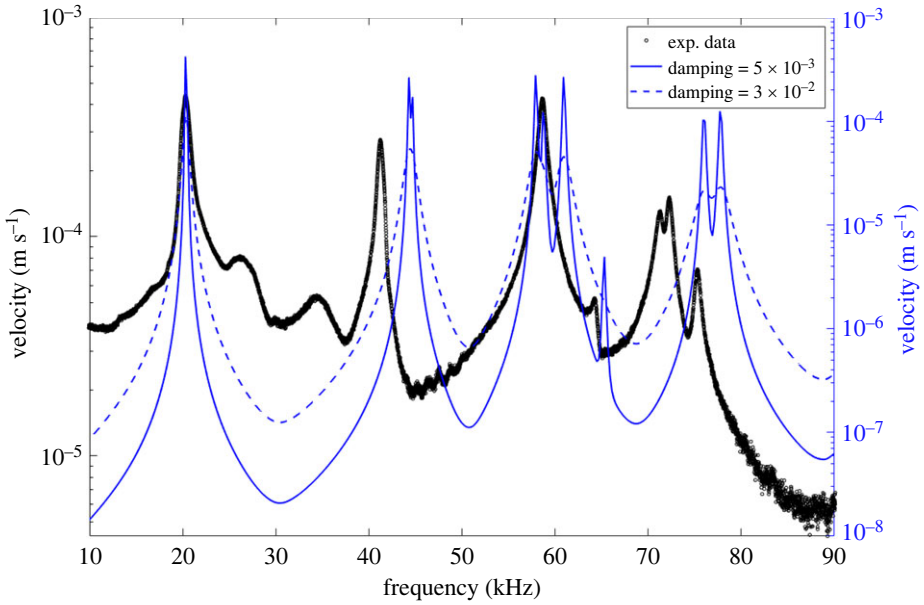

Figure 9. Numerical frequency domain analysis. Black symbols, left axis: Experimental frequency response spectrum of the *Turritellinella* sample TC1. Solid and dashed blue lines, right axis: numerical spectra for loss factors equal to $\eta_s = 5 \times 10^{-3}$ and $\eta_s = 3 \times 10^{-2}$, respectively.

the common basic structural features, i.e. the conical shape. Panels (*b*), (*c*) and (*e*), (*f*) report the first two simulated modal shapes for the cone and the *Turritella*, respectively. Arrows indicating the displacement magnitude and direction are also reported to help the comparison. One can easily see that these two modes present the same vibration characteristics. On the other hand, at higher frequencies, the greater structural complexity of the *Turritella* gives rise to a richer behaviour, with more numerous peaks. These are related to the spiral, hierarchical structure of the real shell, with several more modes occurring above 100 kHz. Moreover, by comparing modes that are rather close in frequency, we can observe a more complex deformation behaviour for the shell. For example, panels (*d*) and (*g*) show two high-frequency modes for the cone and the shell at approximately 162 and 166 kHz, respectively. Both modes reported in panels (*d*) and (*g*) feature a mixed behaviour but, while the former, belonging to the cone, has a dominant bending contribution along with torsional components, the mode of the *Turritella* also displays non-negligible longitudinal components, indicated by the vertical arrows, together with more pronounced torsional effects than for the conical structure.

The shell has a protective function, and one possible protection is against impacts or dynamic loads, caused either by collisions with hard surfaces such as rocks, or by strikes due to the attack of predators. One way to achieve efficient protection against impacts is to provide a hard and strong surface that can also efficiently dissipate vibrations, i.e. elastic energy. The exceptionally performing capabilities of seashells' microstructure in attenuating impacts have been extensively investigated in the literature, as also reported in the Introduction. It has also been shown that the shell macrostructure and complex geometry can play a significant role in the protective functionality of the shell [40]. However, we can speculate here that the overall dynamical behaviour of the structure, shown in figure 10, can also help to achieve a better performance in terms of impact absorption, since a higher modal density, i.e. a larger number of modes in the same frequency range, featured by the *Turritella* shell structure, indicates the presence of more equivalent spring/damper subsystems in the system and thus a greater efficiency in the capability of storing (and dissipating) strain energy, and therefore possibly a more resilient structure to impacts. Indeed, any external dynamic load, e.g. an impact, will include a wide-band frequency spectrum, and distribute its energy most efficiently among all the modes activated in the excited structure. An analogy could be made with the specific heat of a solid where the phonon density of states corresponds to the resonance spectrum in the shell. The energy exchanged as heat by the solid is the temperature derivative of the integral over the phonon spectrum of the normal mode energy [59]. Likewise, in the shell, the stored elastic energy is dissipated over the impact duration. Therefore, the higher the modal density, the more efficient will be the energy spread. The limit case is that of an impulse modelled as a Dirac delta: its frequency spectrum is a constant and thus will excite the whole spectrum of the shell dividing its total energy among all modes. Moreover, the lowest vibration modes, which in the considered case occur at kHz frequencies, are those at which most of the elastic energy is stored, and therefore dissipated, since these modes generally have the largest vibration amplitudes. Thus, efficient vibration and dissipation at kHz frequencies is probably related to the protective function of the shell in terms of dynamic loads. Finally, it is also interesting to observe that organisms with orthoconical shells belonging to the same phylum existed in the past (for example, the extinct nautiloid cephalopod *Orthoceras* [60]), but these were part of a taxon of nektonic animals, occupying a different biotype from that of the *Turritella*.

As an additional feature, we notice that most of the energy is focused on the shell apex, i.e. far from where the animal lives. Electronic supplementary material, figure S11, shows the magnitude of the velocity amplitude from the bottom to the apex of the shell for the first three resonance modes: the amplitude is noticeably larger at the apex, where most of the energy is directed, in agreement with the protective role of the shell. This fact, which could already be inferred from the displacement field of the modal shapes reported in figure 7,

Downloaded from https://royalsocietypublishing.org/ on 03 August 2023

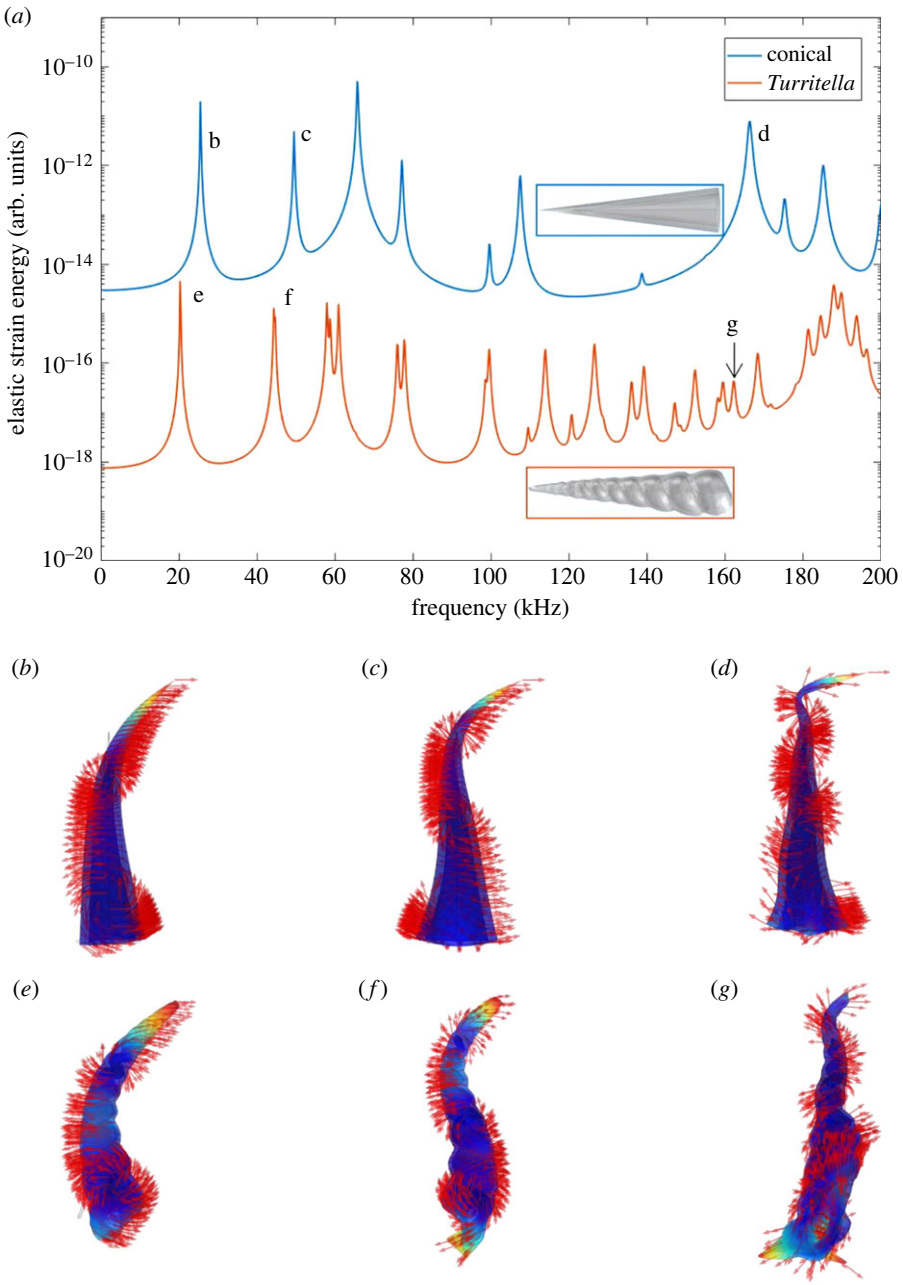

Figure 10. (*a*) Calculated elastic strain energy spectrum for the *Turritellinella* sample TC1 (red) and for an ideal, conical shell (blue) with the same mass and length as the *Turritella*. The loss factor, in both cases, is equal to 5×10^{-3}. The spectrum for the conical shell is shifted upward for clarity. (*b–d*) Numerical modal shapes for the conical shell geometry. Arrows represent displacement. (*b*) First mode at 25.5 kHz, (*c*) second mode at 49.5 kHz, (*d*) higher frequency mode at 166.1 kHz. (*e–g*) Numerical modal shapes for the *Turritella* shell geometry. Arrows represent displacement. (*e*) First mode at 20.3 kHz, (*f*) second mode at 44.3 kHz, (*g*) higher frequency mode at 161.9 kHz.

suggests that the shell structure merits further investigation, to obtain information regarding its possible capability in directional energy flow [61,62], taking also into account that elements with varying cross-section in periodic structures can lead to effective vibration attenuation [63].

4.3. Hierarchical and graded properties

The geometrical structure of the shell also presents a hierarchical configuration, in the sense that the smaller spirals feature on the surface, in their turn, smaller spirals. The geometrical properties of the second-order hierarchy are reported in electronic supplementary material, figure S12. The pitch (distance between two adjacent small whorls on the shell surface) is decreasing towards the apex of the shell. Their thickness has also a slightly decreasing trend towards the apex, thus indicating that the shell features graded properties that are known to give rise to interesting effects on wave propagation [64]. Most probably, the main reason for this geometrical feature, which can be compared to a drill, is to help the organism to burrow under the mud [65]. However, it is also interesting to investigate, as a possible secondary functionality, the effect of this hierarchical structure on the vibrational behaviour of the shell. Thus, the frequency response function of the shell has been calculated and compared up to 400 kHz in the presence of only the first-order of hierarchy and in the presence of both orders. The spectra are reported up to 200 kHz in electronic supplementary material, figure S13. Up to the investigated frequencies, the second-order spirals do not noticeably influence the results, which remain virtually unchanged with or without the

Downloaded from https://royalsocietypublishing.org/ on 03 August 2023

second-order structure. The Young's modulus and Poisson's ratio values that reproduce the experimental spectra remain within the error bar determined from the RUS analysis. The shape and number of peaks in the frequency response function show minimal differences, with just a slight shift in frequency. This is reasonable because, due to the small length scale of these finer structures, their effects are expected to emerge at higher frequencies. At the same time, pushing this kind of analysis above these frequencies makes the interpretation of the results complicated and computationally expensive, due to the much smaller element size required for the mesh, and different methods are therefore needed. In recent years, however, corrugated surfaces (i.e. planar or planar-like structures with periodically varying thickness) have demonstrated to be a viable means to control wave propagation by creating Bragg scattering band gaps, resulting in destructive interference which prohibits wave propagation in certain frequency ranges. This concept has been investigated previously considering beams [66] and plate structures [67], showing also a potential for technological applications [68]. The geometric description of such previously investigated structures is deeply connected to the shell varying-thickness characteristic, thus suggesting the need of a dedicated investigation. This topic, which goes beyond the scope of the present paper, is currently under investigation.

5. Conclusion

In this paper, we have proposed a procedure that integrates microstructural analysis and FEA-based RUS to investigate the mechanical and vibrational properties of biological materials, implementing it on two varieties of seashells. The method allows to perform RUS on biological samples with complex shape and to obtain information not only regarding the frequency spectrum of the various vibrational modes, but also on their specific modal shapes, thus rendering a comparison with numerical data unambiguous. Characterization at the nanoscale reveals the extraordinarily complex microstructure of the shells. In general, this type of analysis can be useful to check the presence of heterogeneity, grading, anisotropy and other mechanical features that might need to be included in macroscopic simulations, such as anisotropic moduli, multi-material components or with spatially graded properties. In this study, it was possible to use homogeneous mechanical properties for the entire structure, but in general, since a direct inclusion of the microstructure is computationally unfeasible, to fill the gap between the properties at the microscale and those at the macroscale, ad hoc multiscale structural models should be designed and used, as has been done for other natural systems [69]. Moreover, homogenization procedures might also be necessary. On the other hand, the results provide a starting guess for the macroscopic parameters to be introduced in the simulations. Here, we did not observe a significant change of the properties along the cross-section of the samples, but the large dispersion of data in the AFM results is an intrinsic effect of the shell microstructure which turned out to be the dominant effect. From the nanoindentation experiments we could obtain the correct order of magnitude of the Young's modulus to insert as a starting value for the FEA. The FEA simulations were performed on the actual shell geometry, as obtained from the CT scan. From the comparison with the experimental resonance frequencies and modal shapes, the mechanical properties that describe the macroscopic behaviour of the structure were determined. The obtained Young's modulus values are within the range obtained by the nanoindentation experiments but differ slightly from sample to sample. Overall, the obtained values are in agreement with those reported in the literature for three-point bending tests on the same type of microstructure.

The dynamic response of the complex structure of the *Turritella* was then compared with that of a simplified, purely conical, shell. It was shown that, in addition to the same vibration modes as the ideal conical one, the real shell features a much richer spectral behaviour, deriving from the greater structural complexity. This could also (but clearly, not exclusively), be related to improved attenuation capabilities of the structure under impacts in terms of an enhanced number of equivalent spring/damper subsystems, i.e. a higher modal density and thus a more efficient distribution of energy for dissipation. Another interesting feature observed is the pronounced directional energy flow towards the apex, which is far from where the animal lives. This fact suggests further investigations in view of applications in wave-beaming devices for directional energy flow. These shells also feature graded properties in their geometrical, hierarchical structure. The effects of the second-order spiral hierarchy, however, are expected to appear at frequencies higher than those considered in this study. Since corrugated surfaces have already shown interesting wave propagation effects such as Bragg scattering and destructive interference over different frequency ranges, investigations are already under way in this regard. Therefore, the above-mentioned characteristics provide us with some interesting guidelines for the design of possible bioinspired devices for wave propagation control.

In summary, it is known that many natural systems that have exceptional impact attenuation properties feature hierarchical, interfacial, porous and composite architectures [5]. In the dynamical analysis reported here, we have shown that the hierarchical and helicoconic characteristics play a significant role in the rich frequency response of the shells. To verify this hypothesis, the method presented here could be implemented in a systematic manner for the characterization of other biological structures of interest for their vibration behaviour, focusing on hierarchical features, allowing to gain further insight into their evolutionary development, to reveal the effect of environmental conditions, like ecological stress, on different samples of shells of the same species and to draw inspiration for efficient impact resistant or vibration damping bioinspired designs.

Ethics. This work did not require ethical approval from a human subject or animal welfare committee.

Data accessibility. Experimental datasets supporting this article are provided as electronic supplementary material.

The data are provided in electronic supplementary material [70].

Authors' contributions. Y.L.: data curation, formal analysis, investigation, methodology; M.L.: conceptualization, formal analysis, investigation, methodology; S.F.S.: formal analysis, investigation; I.C.: formal analysis, investigation; G.G.: formal analysis, investigation, validation, writing—original draft, writing—review and editing; V.F.D.P.: formal analysis; A.S.G.: conceptualization, writing—review and editing; R.M.S.: resources, writing—original draft, writing—review and editing; N.N.: resources, writing—original draft, writing—review and editing; C.V.-B.: resources; N.M.P.: funding acquisition, resources, writing—review and editing; F.B.: conceptualization, funding acquisition, methodology, visualization,

Downloaded from https://royalsocietypublishing.org/ on 03 August 2023

writing—original draft, writing—review and editing; M.T.: conceptualization, data curation, formal analysis, investigation, methodology, project administration, supervision, validation, visualization, writing—original draft, writing—review and editing.

All authors gave final approval for publication and agreed to be held accountable for the work performed therein.

Conflict of interest declaration. We declare we have no competing interests.

Funding. Y.L., M.L., S.F.S., G.G., V.F.D.P., A.S.G., N.M.P., F.B., M.T. acknowledge the European Commission under the FET Open 'Boheme' Grant No. 863179. Y.L. acknowledges financial support provided by the China Scholarship Council (CSC).

Acknowledgements. We thank the Science Museum of Trento (MUSE) for providing the *Turritella terebra* samples. Special thanks to Salvatore Guastella for the SEM images and to J. Pappas and S. Invernizzi for useful discussions.

References

1. Wegst UGK, Bai H, Saiz E, Tomsia AP, Ritchie RO. 2015 Bioinspired structural materials. *Nat. Mater.* **14**, 23–36. (https://doi.org/10.1038/nmat4089)
2. Aizenberg J, Weaver JC, Thanawala MS, Sundar VC, Morse DE, Fratzl P. 2005 Skeleton of *Euplectella* sp.: structural hierarchy from the nanoscale to the macroscale. *Science* **309**, 275–278. (doi:10.1126/science.1112255)
3. Connors M *et al.* 2019 Bioinspired design of flexible armor based on chiton scales. *Nat. Commun.* **10**, 5413. (doi:10.1038/s41467-019-13215-0)
4. Mayer G. 2005 Rigid biological systems as models for synthetic composites. *Science* **310**, 1144–1147 (doi:10.1126/science.1116994)
5. Lazarus BS, Velasco-Hogan A, Gómez-del Río T, Meyers MA, Jasiuk I. 2020 A review of impact resistant biological and bioinspired materials and structures. *J. Mater. Res. Technol.* **9**, 15 705–15 738. (doi:10.1016/j.jmrt.2020.10.062)
6. Bosia F *et al.* 2022 Optimized structures for vibration attenuation and sound control in nature: a review. *Matter* **5**, 3311–3340. (doi:10.1016/j.matt.2022.07.023)
7. Yourdkhani M, Pasini D, Barthelat F. 2010 The hierarchical structure of seashells optimized to resist mechanical threats. *WIT Trans. Ecol. Environ.* **138**, 141–153. (http://doi.org/10.2495/DN100131)
8. Li H, Shen J, Wei Q, Li X. 2019 Dynamic self-strengthening of a bio-nanostructured armor — conch shell. *Mater. Sci. Eng., C.* **103**, 109820. (doi:10.1016/j.msec.2019.109820)
9. Yin Z, Hannard F, Barthelat F. 2019 Impact-resistant nacre-like transparent materials. *Science* **364**, 1260–1263. (doi:10.1126/science.aaw8988)
10. Checa AG. 2018 Physical and biological determinants of the fabrication of Molluscan shell microstructures. *Front. Mar. Sci.* **5**, 353. (doi:10.3389/fmars.2018.00353)
11. Lowenstam HA, Weiner S. 1989 *On biomineralization*. New York, NY: Oxford University Press.
12. Lippmann F. 1973 *Sedimentary carbonate minerals*, 1st edn. Heidelberg, Germany: Springer Berlin.
13. Suzuki M, Nagasawa H. 2013 Mollusk shell structures and their formation mechanism. *Can. J. Zool.* **91**, 349–366. (doi:10.1139/cjz-2012-0333)
14. Levi-Kalisman Y, Falini G, Addadi L, Weiner S. 2001 Structure of the nacreous organic matrix of a bivalve mollusk shell examined in the hydrated state using Cryo-TEM. *J. Struct. Biol.* **135**, 8–17. (doi:10.1006/jsbi.2001.4372)
15. Neves NM, Mano JF. 2005 Structure/mechanical behavior relationships in crossed-lamellar sea shells. *Mater. Sci. Eng., C* **25**, 113–118. (doi:10.1016/j.msec.2005.01.004)
16. Ritchie RO. 2011 The conflicts between strength and toughness. *Nat. Mater.* **10**, 817–822. (doi:10.1038/nmat3115)
17. Currey JD, Kohn AJ. 1976 Fracture in the crossed-lamellar structure of *Conus* shells. *J. Mater. Sci.* **11**, 1615–1623. (doi:10.1007/BF00737517)
18. Kuhn-Spearing LT, Kessler H, Chateau E, Ballarini R, Heuer AH, Spearing SM. 1996 Fracture mechanisms of the *Strombus gigas* conch shell: implications for the design of brittle laminates. *J. Mater. Sci.* **31**, 6583–6594. (doi:10.1007/bf00356266)
19. Kamat S, Su X, Ballarini R, Heuer AH. 2000 Structural basis for the fracture toughness of the shell of the conch *Strombus gigas*. *Nature* **405**, 1036–1040. (doi:10.1038/35016535)
20. Barthelat F, Rim JE, Espinosa HD. 2008 A review on the structure and mechanical properties of mollusk shells – perspectives on synthetic biomimetic materials. In *Applied scanning probe methods XIII: nanoScience and technology* (eds B Bhushan, H Fuchs), pp. 17–44. Berlin, Germany: Springer.
21. Weaver JC *et al.* 2012 The stomatopod dactyl club: a formidable damage-tolerant biological hammer. *Science* **336**, 1275–1280. (doi:10.1126/science.1218764)
22. Wang L, Cheung JTM, Pu F, Li D, Zhang M, Fan Y. 2011 Why do woodpeckers resist head impact injury: a biomechanical investigation. *PLoS ONE* **6**, e26490. (doi:10.1371/journal.pone.0026490)
23. Damiens R, Rhee H, Hwang Y, Park SJ, Hammi Y, Lim H, Horstemeyer MF. 2012 Compressive behavior of a turtle's shell: experiment, modeling, and simulation. *J. Mech. Behav. Biomed. Mater.* **6**, 106–112. (doi:10.1016/j.jmbbm.2011.10.011)
24. Li Y, Ortiz C, Boyce MC. 2012 Bioinspired, mechanical, deterministic fractal model for hierarchical suture joints. *Phys. Rev. E – Stat. Nonlinear. Soft Matter Phys.* **85**, 031901. (doi:10.1103/physreve.85.031901)
25. Gao C, Li Y. 2019 Mechanical model of bio-inspired composites with sutural tessellation. *J. Mech. Phys. Solids* **122**, 190–204. (doi:10.1016/j.jmps.2018.09.015)
26. Pritchard JJ, Scott JH, Girgis FG. 1956 The structure and development of cranial and facial sutures. *J. Anat.* **90**, 73.
27. Migliori A, Sarrao JL, Visscher WM, Bell TM, Lei M, Fisk Z, Leisure RG. 1993 Resonant ultrasound spectroscopic techniques for measurement of the elastic moduli of solids. *Phys. B Phys. Condens. Matter.* **183**, 1–24. (doi:10.1016/0921-4526(93)90048-B)
28. Remillieux MC, Ulrich TJ, Payan C, Rivière J, Lake CR, Le Bas PY. 2015 Resonant ultrasound spectroscopy for materials with high damping and samples of arbitrary geometry. *J. Geophys. Res. Solid Earth* **120**, 4898–4916. (doi:10.1002/2015JB011932)
29. Longo R, Laux D, Pagano S, Delaunay T, Le Clézio E, Arnould O. 2018 Elastic characterization of wood by resonant ultrasound spectroscopy (RUS): a comprehensive study. *Wood Sci. Technol.* **52**, 383–402. (doi:10.1007/s00226-017-0980-z)
30. Longo R, Delaunay T, Laux D, El Mouridi M, Arnould O, Le Clézio E. 2012 Wood elastic characterization from a single sample by resonant ultrasound spectroscopy. *Ultrasonics* **52**, 971–974. (doi:10.1016/j.ultras.2012.08.006)
31. Bernard S, Grimal Q, Laugier P. 2013 Accurate measurement of cortical bone elasticity tensor with resonant ultrasound spectroscopy. *J. Mech. Behav. Biomed. Mater.* **18**, 12–19. (doi:10.1016/j.jmbbm.2012.09.017)
32. Daoui H, Cai X, Boubenider F, Laugier P, Grimal Q. 2017 Assessment of trabecular bone tissue elasticity with resonant ultrasound spectroscopy. *J. Mech. Behav. Biomed. Mater.* **74**, 106–110. (doi:10.1016/j.jmbbm.2017.05.037)
33. Mazzotti M, Sugino C, Kohtanen E, Erturk A, Ruzzene M. 2021 Experimental identification of high order Lamb waves and estimation of the mechanical properties of a dry human skull. *Ultrasonics* **113**, 106343. (doi:10.1016/j.ultras.2020.106343)
34. Wang R, Fan F, Zhang Q, Li X, Niu H, Laugier P. 2019 Elastic constants identification of irregular hard biological tissue materials using FEM-based resonant ultrasound spectroscopy. *J. Mech. Behav. Biomed. Mater.* **96**, 20–26. (doi:10.1016/j.jmbbm.2019.04.031)
35. Nguyen CPT, Schoenherr P, Juli L, Seidel J. 2021 In-depth atomic force microscopy investigation of nanoscale mechanical properties of Pāua nacre. *Nanoscale* **13**, 16 959–16 967. (doi:10.1039/d1nr03469c)
36. Jung JY, Naleway SE, Yaraghi NA, Herrera S, Sherman VR, Bushong EA, Ellisman MH, Kisailus D, McKittrick J. 2016 Structural analysis of the tongue and hyoid

Downloaded from https://royalsocietypublishing.org/ on 03 August 2023

apparatus in a woodpecker. *Acta Biomater.* **37**, 1–13. (doi:10.1016/j.actbio.2016.03.030)

37. Jung JY, Pissarenko A, Yaraghi NA, Naleway SE, Kisailus D, Meyers MA, McKittrick J. 2018 A comparative analysis of the avian skull: woodpeckers and chickens. *J. Mech. Behav. Biomed. Mater.* **84**, 273–280. (doi:10.1016/j.jmbbm.2018.05.001)
38. Presser V, Gerlach K, Vohrer A, Nickel KG, Dreher WF. 2010 Determination of the elastic modulus of highly porous samples by nanoindentation: a case study on sea urchin spines. *J. Mater. Sci.* **45**, 2408–2418. (doi:10.1007/s10853-010-4208-y)
39. Losic D, Short K, Mitchell JG, Lal R, Voelcker NH. 2007 AFM nanoindentations of diatom biosilica surfaces. *Langmuir* **23**, 5014–5021. (doi:10.1021/la062666y)
40. Rajabi H, Darvizeh A, Shafiei A, Eshghi S, Khaheshi A. 2014 Experimental and numerical investigations of *Otala lactea*'s shell – I. Quasi-static analysis. *J. Mech. Behav. Biomed. Mater.* **32**, 8–16. (doi:10.1016/j.jmbbm.2013.12.008)
41. Chen DA, Klotz LE, Ross BE. 2016 Mathematically characterizing natural systems for adaptable, biomimetic design. *Procedia Eng.* **145**, 497–503. (doi:10.1016/j.proeng.2016.04.031)
42. Chen DA, Ross BE, Klotz LE. 2018 Parametric analysis of a spiraled shell: learning from nature's adaptable structures. *Designs* **2**, 46. (doi:10.3390/designs2040046)
43. Chen DA 2016 The adaptable growth of seashells: informing the design of the built environment through quantitative biomimicry. *All Dissertations*. 1740. See https://tigerprints.clemson.edu/all_dissertations/1740.
44. Pappas JL, Miller DJ. 2013 A generalized approach to the modeling and analysis of 3D surface morphology in organisms. *PLoS ONE* **8**, e77551. (doi:10.1371/journal.pone.0077551)
45. Deng X *et al.* 2021 Topographically guided hierarchical mineralization. *Mater. Today Bio.* **11**, 100119. (doi:10.1016/j.mtbio.2021.100119)
46. Oliver WC, Pharr GM, Introduction I. 1992 An improved technique for determining hardness and elastic modulus using load and displacement sensing indentation experiments. *J. Mater. Res.* **7**, 1564–1583. (doi:10.1557/JMR.1992.1564)
47. Hertz H. 1882 Ueber die Berührung fester elastischer Körper. *J fur die Reine und Angew Math.* **1882**, 156–171. (doi:10.1515/crll.1882.92.156)
48. Butt HJ, Cappella B, Kappl M. 2005 Force measurements with the atomic force microscope: technique, interpretation and applications. *Surf. Sci. Rep.* **59**, 1–152. (doi:10.1016/j.surfrep.2005.08.003)
49. Stassi S, Cooperstein I, Tortello M, Pirri CF, Magdassi S, Ricciardi C. 2021 Reaching silicon-based NEMS performances with 3D printed nanomechanical resonators. *Nat. Commun.* **12**, 6080. (doi:10.1038/s41467-021-26353-1)
50. Chen CC, Lin CC, Liu LG, Sinogeikin SV, Bass JD. 2001 Elasticity of single-crystal calcite and rhodochrosite by Brillouin spectroscopy. *Am. Mineral.* **86**, 1526–1529. (doi:10.2138/am-2001-11-1222)
51. Kearney C, Zhao Z, Bruet BJF, Radovitzky R, Boyce MC, Ortiz C. 2006 Nanoscale anisotropic plastic deformation in single crystal aragonite. *Phys. Rev. Lett.* **96**, 255505. (doi:10.1103/PhysRevLett.96.255505)
52. Luo C, Yang X, Li J. 2022 Mechanical properties of single-crystal calcite and their temperature and strain-rate effects. *Materials (Basel)* **15**, 4613. (doi:10.3390/ma15134613)
53. Urey HC, Lowenstam HA, Epstein S, Mckinney CR. 1951 Measurement of paleotemperatures and temperatures of the upper cretaceous of England, Denmark, and the southeastern United States. *Bull. Geol. Soc. Am.* **62**, 399–416.
54. Nielsen C. 2004 Trochophora larvae: cell-lineages, ciliary bands, and body regions. 1. Annelida and Mollusca. *J. Exp. Zool. B: Mol. Dev. Evol.* **302**, 35–68. (doi:10.1002/jez.b.20001)
55. Lorrain A, Gillikin DP, Paulet YM, Chauvaud L, Le Mercier A, Navez J, André L. 2005 Strong kinetic effects on Sr/Ca ratios in the calcitic bivalve *Pecten maximus*. *Geology* **33**, 965–968. (doi:10.1130/G22048.1)
56. Yoshimura T, Nakashima R, Suzuki A, Tomioka N, Kawahata H. 2010 Oxygen and carbon isotope records of cultured freshwater pearl mussel *Hyriopsis* sp. shell from Lake Kasumigaura, Japan. *J. Paleolimnol.* **43**, 437–448. (doi:10.1007/s10933-009-9341-8)
57. Currey JD, Taylor JD. 1974 The mechanical behaviour of some molluscan hard tissues. *J. Zool.* **173**, 395–406. (doi:10.1111/j.1469-7998.1974.tb04122.x)
58. Currey JD. 1976 Further studies on the mechanical properties of mollusc shell material. *J. Zool.* **180**, 445–453. (doi:10.1111/j.1469-7998.1976.tb04690.x)
59. Von Ashcroft NW, Mermin ND. 1976 *Solid state physics*. New York, NY: Saunders College Publishing.
60. Kröger B. 2004 Revision of Middle Ordovician orthoceratacean nautiloids from Baltoscandia. *Acta Palaeontol Pol.* **49**, 57–74.
61. Ruzzene M, Scarpa F, Soranna F. 2003 Wave beaming effects in two-dimensional cellular structures. *Smart Mater. Struct.* **12**, 363. (doi:10.1088/0964-1726/12/3/307)
62. Zelhofer AJ, Kochmann DM. 2017 On acoustic wave beaming in two-dimensional structural lattices. *Int. J. Solids Struct.* **115–116**, 248–269. (doi:10.1016/j.ijsolstr.2017.03.024)
63. Dal Poggetto VF, Bosia F, Miniaci M, Pugno NM. 2021 Band gap enhancement in periodic frames using hierarchical structures. *Int. J. Solids Struct.* **216**, 68–82. (doi:10.1016/j.ijsolstr.2021.01.003)
64. Ma F, Wu JH, Huang M, Fu G, Bai C. 2014 Cochlear bionic acoustic metamaterials. *Appl. Phys. Lett.* **105**, 213702. (doi:10.1063/1.4902869)
65. Trueman ER, Brown AC. 1992 The burrowing habit of marine gastropods. *Adv. Mar. Biol.* **28**, 389–431. (doi:10.1016/S0065-2881(08)60041-3)
66. Pelat A, Gallot T, Gautier F. 2019 On the control of the first Bragg band gap in periodic continuously corrugated beam for flexural vibration. *J. Sound Vib.* **446**, 249–262. (doi:10.1016/j.jsv.2019.01.029)
67. Dal Poggetto VF, Arruda JdF. 2021 Widening wave band gaps of periodic plates via shape optimization using spatial Fourier coefficients. *Mech. Syst. Signal. Process.* **147**, 107098. (doi:10.1016/j.ymssp.2020.107098)
68. Ciampa F, Mankar A, Marini A. 2017 Phononic crystal waveguide transducers for nonlinear elastic wave sensing. *Sci. Rep.* **7**, 14712. (doi:10.1038/s41598-017-14594-4)
69. Bar-On B, Barth FG, Fratzl P, Politi Y. 2014 Multiscale structural gradients enhance the biomechanical functionality of the spider fang. *Nat. Commun.* **5**, 3894. (doi:10.1038/ncomms4894)
70. Liu Y *et al*. 2023 Multiscale static and dynamic mechanical study of the *Turritella terebra* and *Turritellinella tricarinata* seashells. Figshare. (doi:10.6084/m9.figshare.c.6743105)